We are IntechOpen, the world's leading publisher of Open Access books
Built by scientists, for scientists

4,800
Open access books available

122,000
International authors and editors

135M
Downloads

Our authors are among the

154
Countries delivered to

TOP 1%
most cited scientists

12.2%
Contributors from top 500 universities

WEB OF SCIENCE™

Selection of our books indexed in the Book Citation Index
in Web of Science™ Core Collection (BKCI)

Interested in publishing with us?
Contact book.department@intechopen.com

Numbers displayed above are based on latest data collected.
For more information visit www.intechopen.com

Methods and performances for multi-pass SAR Interferometry

Stefano Tebaldini and Andrea Monti Guarnieri
Dipartimento di Elettronica e Informazione
Politecnico di Milano
Piazza Leonardo da Vinci, 32
20133 MILANO

1. Introduction

Thanks to the several space missions accomplished since ERS-1, the scientific community has been provided with a huge amount of data suitable for interferometric processing. The innovation was the availability of multiple compatible images of the same areas. Such images, achieved by looking from slightly different point of view different orbits, and/or by different frequencies, and/or at different times, has largely extended the capabilities of InSAR with respect to the traditional dual image case. The advantage granted by the possibility to form multiple interferograms, instead than just one, is two folded. On the one hand, the estimation of the parameters of interest, be them related to the DEM or the terrain deformations, is driven by a larger data set, resulting in more accurate estimates. On the other hand, new parameters may be added to the set of the unknowns, allowing to study complex phenomena, such as the temporal evolution of the atmospheric and deformation fields. A major issue with multi-image InSAR is that targets are, in general, affected by temporal and spatial decorrelation phenomena, which hinders the exploitation of large spatial and/or temporal baselines. For this reason, most of literature about multi-image InSAR has focused mainly on *targets that stay coherent in all the acquisitions*, which has resulted in a substantial lack of a systemic approach to deal with decorrelating targets in the field of InSAR.

The aim of this chapter is to propose a general approach to exploit all the available information, that is the stack of interferometric SAR images, and that formally accounts for the impact of target decorrelation. This approach is based on the optimal estimate of the data in a statistical sense. The basic idea is to split the estimation process into two steps. In the first step, a maximum likelihood (ML) estimator is used that jointly exploits all the $N \times (N-1)/2$ interferograms available with N acquisitions, in order to yield the best estimates of the $N-1$ phases that correspond to the optical path differences between the target and the sensors. Target decorrelation is accounted for by properly weighting each interferogram in dependence on the target statistics. The estimated phases will be referred to as Linked Phases, to remind that these terms are the result of the joint processing of all the $N(N-1)/2$ interferograms. Once the first estimation step has yielded the estimates of the interferometric phases, the second step is required to separate the contributions of the APSs and the decorrelation noise from the parameters of interest, such as the Line of Sight Deformation Field (LDF) and the topography.

The same two-step approach can be followed to derive the performances of the Multi-Baseline Interferometry, in the frame of the Hybrid Cramér Rao Bound (HCRB) that we will discuss in this same chapter.

2. A brief review of multi-image InSAR techniques

2.1 Permanent Scatterers Interferometry (PSI)

This approach, developed by *Ferretti et al.*(1), represents the first attempt to give a formal framework to the problem of multi-baseline InSAR. The analysis is based on the selection of a number of highly coherent, temporally stable, point-like targets within the imaged scene, which may be identified by analyzing the amplitude time series extracted from the whole set of images in correspondence with every pixel (2), (3), (4). Such targets, named Permanent Scatterers (PS), are typically represented by man made objects, but also isolated trees or stable rocks may serve as PSs. However, the highest density of PSs is expected to be found within urban areas. For every selected PS the time series of the phase differences of every image with respect to a reference one is extracted. Since the selected targets are by definition the ones which remain coherent in all of the images, it can be assumed that no decorrelation phenomena occur. Therefore, the phase difference time series may be effectively represented by a linear model plus noise. At this point, an effective separation of the various contributions, such as topography, displacement rate, and APSs, may be carried out by exploiting the time-space statistical properties of each. In this sense, this approach is similar to Wiener filtering, and could be in principle solved by such technique. However, because of the high computational burden and the non linearity due to the 2π ambiguity, *Ferretti et al.* proposed instead an iterative algorithm, involving 2D frequency estimation, phase unwrapping and linear filtering (5). The main limitation within this approach lies in the sparsity of the grid for the selected PS. To overcome this limitation, a second step is performed, consisting in resampling the APSs estimates on the uniform image grid, remove these terms, and look for a more dense set of PSs basing on phase stability, rather than amplitude. This process, however, is likely to fail in areas where the initial PS selection, based on amplitude stability, does not suffice to cover the whole imaged scene, as it may be the case of non urban areas, especially for data set suffering from amplitude calibration problems. A first solution to this problem has been proposed by *Hooper et al.* (6), who defined an iterative point selection algorithm basing directly on a phase stability criterion. The selected point are called Persistent Scatterers. This method has been shown to yield a more dense point grid on rock areas than the amplitude based algorithms exploited in PSI.

2.2 Techniques based on interferogram selection

Several approaches have been presented in literature to perform SAR interferometric analysis over scenes where the PS assumption may not be retained. A number of these works share the idea to minimize the effect of target decorrelation by forming the interferograms from properly selected pairs, rather than with respect to a fixed reference image, as done in PS processing. Despite the good results achieved in the applications, however, there's no clear and formal assessment of the criteria which should drive the selection of the image pairs to be used. As a result, the processing is heuristically based on the exploitation of a set of interferograms taken with the shortest temporal and/or spatial baselines possible (7), (8), (6).

2.3 The Small Baseline Subsets (SBAS) approach

A more sophisticated approach is the one by *Berardino et al.*, exploiting the concept of Small Baseline Subsets (SBAS) (9), (10). This approach may be somehow considered as the complement of the PS approach. While the latter looks for targets which remain coherent throughout the whole data set, the SBAS algorithm tries to extract information basing on every single interferogram available. The algorithm accounts for spatial decorrelation phenomena by partitioning the data set into a number of subsets, each of which is constituted by images acquired from orbits close to each other. In this way, interferograms corresponding to large baselines are discarded. After unwrapping the phases of the interferograms within the subsets, the estimation of the physical quantities of interest, such as the topographic profile and the deformation field, is carried out through singular value decomposition. The choice of this inversion technique accounts for the rank deficiency caused by partitioning the data set into subsets, resulting in the solution being chosen on the basis of a minimum norm criterion. Further processing, similar to that indicated in (5), carries out the removal of the atmospheric artifacts.

2.4 Maximum Likelihood Estimation Techniques

The application of Maximum Likelihood Estimation techniques for InSAR processing has been considered by *Fornaro et al* (11), *De Zan* (12), *Rocca* (13), and in two works by *Tebaldini and Monti Guarnieri* (14), of which this chapter represents an extension. The rationale of ML techniques, as applied to InSAR, is to exploit target statistics, represented by the ensemble of the coherences of every available interferogram, to design a statistically optimal estimator for the parameters of interest. An advantage granted by these techniques is that the criteria which determine the role of each interferogram in the estimation process are directly derived from the coherences, through a rigorous mathematical approach. Furthermore, by virtue of the properties of the ML estimator (MLE), the estimates of the parameters of interest are asymptotically (we.e. large signal to noise ratio, large data space) unbiased an minimum variance. On the other hand, a common drawback of these techniques is the need for a reliable information about target statistics, required to drive the estimation algorithm. The main differences among the works by *De Zan*, *Rocca*, and the one to be depicted in this chapter are relative to the initial parametrization of the data statistics. The ML approach proposed by *De Zan* consists in estimating residual topography and LOS subsidence rate directly from the data. Conversely, in the work by *Rocca* (13), similarly to the approach within this chapter, the estimation process is split into two steps, in that first $N(N-1)/2$ interferograms are formed out of N acquisitions, and then the second order statistics of the interferograms are exploited to derive the optimal linear estimator of the parameters of interest, under the small phase approximation. After the Extended Invariance Principle (EXIP), it follows that the condition under which the splitting of the MLE into two steps does not entail any loss of information about the original parametrization of the problem, θ, is that the covariance of the estimate errors committed in the first step actually approaches the CRB. Therefore, the estimation of topography and Line Of Sight (LOS) subsidence rate directly from the data proposed by *De Zan* in (12), is intrinsically the most robust, since the estimation of the whole structure of the model is performed in a single step. This approach, however, would result in an overwhelming computational burden if applied to a large set of parameters. On the contrary, in the approach followed by *Rocca*, (13), the first step may be interpreted as a totally unstructured estimation of the model, since each of the $N(N-1)/2$ phases of all the available interferograms is estimated separately. It follows that the computational burden is kept very low, but the performance of the one step ML estimator may be approached only under the condition that the $N(N-1)/2$

phases are estimated with sufficient accuracy, as it happens by exploiting a large estimation window and/or at high SNR (Signal To Noise Ratio). Finally, the two step estimator to be depicted in this chapter may be placed in between the two solutions here exposed, the first step being devoted to carrying out a joint estimation of $N-1$ phases from the data. This solution corresponds to the estimation of a weak structured model, based on the hypothesis of phase triangularity herewith discussed.

3. Model for the multi-pass observations of a single target

Let us consider the multibaseline geometry in Fig. 1: this geometry is fairly conventional, and the reader is referred to like (15–17) for a general view of SAR interferometry, or (18) for a tutorial. The same target P is observed by a set on N sensors in different parallel tracks or, identically, by N repeated acquisitions of the same sensor. Each observation is focused getting an high resolution image of the whole scene. Two complex focused images can be combined to compute the interferogram, that their Hermitian. The interferogram phase, shown in Fig. 1 on the right, is proportional to the resultant of the travel phase difference between the two acquisitions and the difference between the Atmospheric Phase Screen (APS) of the two acquisitions:

$$
\begin{aligned}
\varphi_{nm} &= \varphi_n - \varphi_m \\
&= \left(\frac{4\pi}{\lambda} R_n(P) + \alpha(n) \right) - \left(\frac{4\pi}{\lambda} R_m(P) + \alpha(m) \right),
\end{aligned}
\tag{1}
$$

$R_n(P)$ and $R_m(P)$ being respectively the slant range of the n-th and m-th antennas to the target point P, and $\alpha(n)$, $\alpha(m)$ the phase errors due to the propagation in the atmosphere in the two acquisitions(19). In turn, the slant range can be thought of a fixed contribution, due to topography, and a time-varying LOS displacement. As an example, for a linear deformation:

$$
R_n(P) = R_{n0} + v(P) \cdot t_n
$$

$v(P)$ being the Linear Deformation Rate and t_n the time of the n-th acquisition.

The interferogram phases keeps then information on both the geometry of the system, that depends on the topography, hence the DEM, and the a possible Line Of Sight displacement of the target in the time between the two acquisitions. In the following, we assume that all the focused images are coregistered on the same range, azimuth reference of one image, that we will define as the master image, so that the same target contributes in the same pixels of all the N images in the stack (18).

3.1 Single target model

We assume that each pixel in the SAR images is described by a distributed target, i.e., the contributions of many independent scatterers in the resolution cell. The result is a realization of a stochastic process, whose pdf conditioned on the interferometric phases may be regarded as being a zero-mean, multivariate circular normal distribution (15). Therefore, the ensemble of the second order moments represents a sufficient statistics to infer information from the data. With reference to a particular location in the slant range - azimuth plane, the expression of the second order moment for the $nm - th$ interferometric pair may be expressed, under the assumption of phase triangularity, as:

$$
E \left[y_n y_m^* \right] = \gamma_{nm} \exp \left(j \left(\varphi_n - \varphi_m \right) \right)
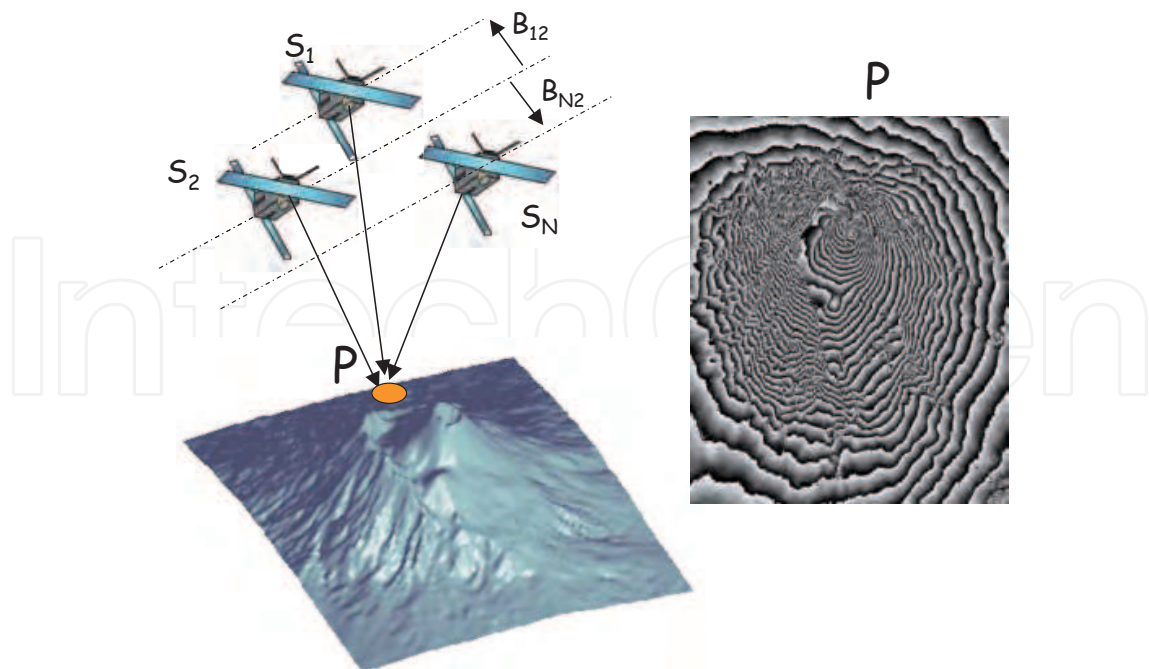\tag{2}
$$

where:

Fig. 1. Interferometric SAR geometry: N sensors, at same azimuth position are shown on the left. On the right, the interferogram's phases obtained by combining two images are shown.

- y_n represents a pixel in the $n - th$ SLC SAR image at the considered slant range - azimuth location;

- γ_{nm} is the coherence of the $nm - th$ interferometric pair; $\gamma_{nn} = 1$ for every n;

- φ_n is the interferometric phase for the $n - th$ acquisition.

Note that the images are supposed to be normalized such that $E\left[|y_n|^2\right] = 1 \, \forall \, n$.
Following (1), the interferometric phases will be expressed in vectors as:

$$\boldsymbol{\varphi} = \boldsymbol{\psi}\left(\boldsymbol{\theta}\right) + \boldsymbol{\alpha} \tag{3}$$

where:

- $\boldsymbol{\varphi} = \left[\begin{array}{ccc} \varphi_0 & ... & \varphi_{N-1} \end{array}\right]^T$ is the vector of the interferometric phases, with respect to an arbitrary reference;

- $\boldsymbol{\theta}$ is the vector of the unknown parameters which describe the LDF and residual topography to be estimated;

- $\boldsymbol{\psi}\left(\boldsymbol{\theta}\right) = \left[\begin{array}{ccc} \psi_0\left(\boldsymbol{\theta}\right) & ... & \psi_{N-1}\left(\boldsymbol{\theta}\right) \end{array}\right]^T$ is a vector of known functions of $\boldsymbol{\theta}$;

- $\boldsymbol{\alpha} = \left[\begin{array}{ccc} \alpha_0 & ... & \alpha_{N-1} \end{array}\right]^T$ represent the atmospheric fields, or APS, affecting the N acquisitions.

The APS may be modeled as a stochastic process, highly correlated over space and uncorrelated from one acquisition to the other, at least under the assumption that SAR images are taken with a repeat interval longer than one day (19; 20). Furthermore, we will here force the

hypothesis that the ensemble of the APSs may be modeled as a normal, zero mean stochastic process with variance σ_α^2:

$$\boldsymbol{\alpha} \quad \sim \quad N\left(\mathbf{0}, \mathbf{R}_\alpha\right) \tag{4}$$
$$\mathbf{R}_\alpha \quad = \quad \sigma_\alpha^2 \mathbf{I}_N$$

where $\mathbf{I}_N$ is the $N \times N$ identity matrix. The reason for this assumption is that it will allow to reach a simple analytical form to lower bound the estimate accuracy. Otherwise, the estimate accuracy would depend not only on the APS variance, but also on the shape of its distribution. As a first approximation, however, this assumption may be retained (21). Note that the characterization of the APS as a zero mean process is clearly unphysical, since the propagation through the atmosphere should result in an additional delay of the received echoes, therefore giving rise to a bias. Such bias, however, is automatically canceled by evaluating the phase differences, $\varphi_n - \varphi_m$, in such a way that model (4) can be retained in the framework of InSAR analyses. As a further remark, note that the assumption that the APSs are uncorrelated from an acquisition to another is not strictly necessary for the theoretical developments to follow.

The set of the coherences, γ_{nm}, of each interferometric pair accounts for decorrelation sources like superficial, volumetric, temporal, etc, is the following product form, suggested in (22):

$$\gamma_{nm} = \gamma_0 \gamma_{nm}^{(sup)} \gamma_{nm}^{(vol)} \gamma_{nm}^{(temp)} \tag{5}$$

Model (2) may be expressed in a conveniently compact form as:

$$\mathbf{R} \overset{def}{=} E\left[\mathbf{y}\mathbf{y}^H\right] = \boldsymbol{\phi}\boldsymbol{\Gamma}\boldsymbol{\phi}^H \tag{6}$$

where:

- $\mathbf{R}$ is the data covariance matrix.
- $\mathbf{y} = \begin{bmatrix} y_0 & \cdots & \cdots & y_{N-1} \end{bmatrix}^T$ is the stack of the SLC images at a given location, (r, x), in the slant range, azimuth plane;
- $\boldsymbol{\Gamma}$ is an $N \times N$ symmetric matrix whose elements are given by the interferometric coherences: $\{\boldsymbol{\Gamma}\}_{nm} = \gamma_{nm}$;
- $\boldsymbol{\phi}$ is an $N \times N$ diagonal matrix whose elements are given by the interferometric phases:

$$\boldsymbol{\phi} = \operatorname{diag}\left\{ \exp\left(j\varphi_0\right) \quad \cdots \quad \cdots \quad \exp\left(j\varphi_{N-1}\right) \right\}$$

Throughout this chapter we will assume that the estimation of the parameters of interest is performed by exploiting **a conveniently small estimation window**, Ω. The pdf of the data sample within the estimation window will be expressed as:

$$p\left(\mathbf{y}_\Omega | \boldsymbol{\varphi}\right) = \text{const} \cdot \prod_{l=1}^{L} \exp\left(-\mathbf{y}^H\left(r_l, x_l\right) \boldsymbol{\phi}\boldsymbol{\Gamma}^{-1}\boldsymbol{\phi}^H \mathbf{y}\left(r_l, x_l\right)\right) \tag{7}$$

where (r_l, x_l) denote the location in the slant range, azimuth plane and L is the number of pixels within the estimation window.
Expression (7) is conditioned to two hypothesis: the stationarity and the incorrelation of the pixels in the window. The hypothesis of stationarity requires that the unknowns, $\boldsymbol{\theta}$, the APSs, $\boldsymbol{\alpha}$, and the coherences, γ_{nm}, are constant inside Ω. Therefore, in practical applications this hypothesis may be retained provided that Ω is small. The hypothesis that no correlation exists among neighboring pixels requires that either one of these two conditions is met:

- all the pixels within the estimation window are referred to the same slant range location;
- the normal baselines are small, in such a way as not to give rise to correlation among neighboring pixels.

Note that the latter represent the most suitable condition for estimating the LDF, which makes it sensible to retain its validity, especially in light of the capabilities which will be provided by the next generation of spaceborne SARs (13). As a first approximation, however, the effect of a non null normal baseline set can be included by letting the correlation coefficients γ_{nm} account for the contribution of spatial decorrelation.

4. Performances estimation in Multi Baseline Interferometry

This section is dedicated to multi-baseline SAR Interferometry (InSAR). We will associate In-SAR with the hypothesis that a single target, either point-like or distributed, is present within the SAR slant range, azimuth resolution cell.
The aim here is to derive a lower bounds of the performance achievable by spaceborne InSAR as for the estimation of the LOS deformation field (LDF) from acquisitions over scenes characterized by a distributed scattering mechanism, such as forests, agricultural fields, soil or rock surfaces, and even ice shelves. Mainly two factors affect the accuracy of InSAR estimates. One arises from decorrelation phenomena among SAR images, due to the spatial structure and temporal behavior of the targets. The other is given by the presence of uncompensated propagation disturbances. As long as spaceborne applications are considered, it is reasonable to assume that uncompensated propagation disturbances are mainly caused by atmospheric fluctuations, and hence in this chapter propagation disturbances will be identified with the Atmospheric Phase Screens (APSs). The ensemble of target decorrelation and APS results in a non Gaussian distribution of the data, which complicates the a-priori assessment of the LDF estimator performance for any given scenario. In the existing literature the computation of InSAR lower bounds is commonly approached as the problem of estimating a set of deterministic parameters in presence of decorrelation noise (23), (24), whereas the role of the APS is in general neglected. Within this chapter it will be shown that, under the hypothesis that a single, distributed, target is present within the SAR resolution cell, the roles of target decorrelation and APSs may be jointly treated by exploiting the Hybrid Cramér-Rao Bound (HCRB), where the unknowns are both deterministic parameters and stochastic variables. This approach results in a compact formulation of the problem, from which it is possible to achieve some closed-form formulas that constitute a useful tool for system design and tuning (25).

4.1 The Hybrid Cramér-Rao bound for InSAR
The data formulation described in the previous section is suited for exploiting the Hybrid Cramér-Rao Bound (HCRB) for lower bounding the accuracy on the estimate of θ. The HCRB (26), (27), (28) applies in the case where some of the unknowns are deterministic and others are random; it unifies the deterministic and Bayesian CRB in such a way as to simultaneously bound the covariance matrix of the unbiased estimates of the deterministic parameters and the mean square errors on the estimates of the random variables (26), (27).
Let $\widehat{\theta}$ be an unbiased estimator of the deterministic parameters θ, and denote $\widehat{\alpha}$ an estimator of the random variables α. The HCRB assures that, for every estimator,

$$E_{\mathbf{y},\alpha}\left[\begin{array}{cc} \left(\widehat{\theta}-\theta\right)\left(\widehat{\theta}-\theta\right)^T & \left(\widehat{\theta}-\theta\right)\left(\widehat{\alpha}-\alpha\right)^T \\ \left(\widehat{\alpha}-\alpha\right)\left(\widehat{\theta}-\theta\right)^T & \left(\widehat{\alpha}-\alpha\right)\left(\widehat{\alpha}-\alpha\right)^T \end{array}\right] \geq \mathbf{J}^{-1} \tag{8}$$

where $E_{\mathbf{y},\boldsymbol{\alpha}}[\ldots]$ denotes expectation with respect to the joint pdf of the data and the APS, $p(\mathbf{y},\boldsymbol{\alpha}|\boldsymbol{\theta})$, and the inequality means that the difference between the left and the right sides of (8) is a nonnegative definite matrix. The matrix $\mathbf{J}$ is called the Hybrid Information Matrix (HIM). It may be obtained as the sum of the standard Fisher Information Matrix (FIM), $\mathbf{F}$, averaged with respect to α, and the prior information matrix $\mathbf{I}_{\boldsymbol{\alpha}}$.

$$\mathbf{J} = E_{\boldsymbol{\alpha}}[\mathbf{F}] + \mathbf{I}_{\boldsymbol{\alpha}} \tag{9}$$

Define $\Delta_{\mathbf{x}}^{\mathbf{y}}$ as a matrix of the second order partial derivatives with respect to two multidimensional variables $(\mathbf{x},\mathbf{y})$:

$$\left\{\Delta_{\mathbf{x}}^{\mathbf{y}}\right\}_{nm} = \frac{\partial^2}{\partial x_n \partial y_m} \tag{10}$$

Then, the matrices $\mathbf{F}$ and $\mathbf{I}_{\boldsymbol{\alpha}}$ are given by:

$$\mathbf{F} = -E_{\mathbf{y}|\boldsymbol{\alpha}}\left\{\begin{bmatrix} \Delta_{\boldsymbol{\theta}}^{\boldsymbol{\theta}} \log p(\mathbf{y}|\boldsymbol{\theta},\boldsymbol{\alpha}) & \Delta_{\boldsymbol{\theta}}^{\boldsymbol{\alpha}} \log p(\mathbf{y}|\boldsymbol{\theta},\boldsymbol{\alpha}) \\ \Delta_{\boldsymbol{\alpha}}^{\boldsymbol{\theta}} \log p(\mathbf{y}|\boldsymbol{\theta},\boldsymbol{\alpha}) & \Delta_{\boldsymbol{\alpha}}^{\boldsymbol{\alpha}} \log p(\mathbf{y}|\boldsymbol{\theta},\boldsymbol{\alpha}) \end{bmatrix}\right\} \tag{11}$$

$$\mathbf{I}_{\boldsymbol{\alpha}} = -E_{\boldsymbol{\alpha}}\left\{\begin{bmatrix} \mathbf{0} & \mathbf{0} \\ \mathbf{0} & \Delta_{\boldsymbol{\alpha}}^{\boldsymbol{\alpha}} \log p(\boldsymbol{\alpha}) \end{bmatrix}\right\} \tag{12}$$

where $E_{\mathbf{y}|\boldsymbol{\alpha}}[\ldots]$ denotes expectation with respect to $p(\mathbf{y}|\boldsymbol{\alpha},\boldsymbol{\theta})$, and $E_{\boldsymbol{\alpha}}[\ldots]$ denotes expectation with respect to $p(\boldsymbol{\alpha})$.

4.1.1 Fisher Information Matrix

Under the assumption that the distribution of the data conditioned on the interferometric is normal it is possible to express the FIM in (11) in a relatively simple form, by exploiting the result:

$$E_{\mathbf{x}|\boldsymbol{\tau}}\left[\frac{\partial^2(\log(p(\mathbf{x}|\boldsymbol{\tau})))}{\partial \tau_n \partial \tau_m}\right] = trace\left\{\frac{\partial \mathbf{R}}{\partial \tau_n}\frac{\partial \mathbf{R}^{-1}}{\partial \tau_m}\right\} \tag{13}$$

that holds for any process distributed as $\mathbf{x} \sim N(\mathbf{0},\mathbf{R}(\boldsymbol{\tau}))$, where $\boldsymbol{\tau}$ is an arbitrary set of coefficients that parameterize the covariance matrix of $\mathbf{x}$.

From (11) and (13), a straightforward application of the chain rule leads to the following expression for the FIM:

$$\mathbf{F} = \begin{bmatrix} \boldsymbol{\Theta}^T \mathbf{X} \boldsymbol{\Theta} & \boldsymbol{\Theta}^T \mathbf{X} \\ \mathbf{X}\boldsymbol{\Theta} & \mathbf{X} \end{bmatrix} \tag{14}$$

where $\boldsymbol{\Theta}$ is the matrix of the first order partial derivatives of the set of functions $\{\psi_n(\boldsymbol{\theta})\}_{n=0}^{N-1}$ with respect to $\boldsymbol{\theta}$,

$$\{\boldsymbol{\Theta}\}_{nm} = \frac{\partial \psi_n(\boldsymbol{\theta})}{\partial \theta_m}, \tag{15}$$

and $\mathbf{X}$ is an $N \times N$ matrix representing the FIM associated to the estimates of the interferometric phases, φ_n. After (13), $\mathbf{X}$ is obtained as:

$$\{\mathbf{X}\}_{nm} = -trace\left\{\frac{\partial \mathbf{R}}{\partial \varphi_n}\frac{\partial \mathbf{R}^{-1}}{\partial \varphi_m}\right\} \tag{16}$$

A straightforward, yet rather long and tedious, evaluation of (16) leads to express $\mathbf{X}$ as:

$$\mathbf{X} = 2L \cdot \left(\boldsymbol{\Gamma} \circ \boldsymbol{\Gamma}^{-1} - \mathbf{I}_N\right) \tag{17}$$

where $\boldsymbol{\Gamma}$ is the coherence matrix in (6), $\circ$ indicates the Hadamard (i.e. entry-wise) product between two matrices and L is the number of (independent) looks inside Ω. The role of $\mathbf{X}$ is to account for the loss of information about the interferometric phases due to target decorrelation. A remarkable property of $\mathbf{X}$ is that its rank is strictly lower than the number of images which constitute the data-set. This fact must not surprise, since the interferometric phases affect the data covariance matrix only through their differences, $\varphi_n - \varphi_m$. Therefore, at least one interferometric phase may be defined arbitrarily. Consider now the case where the data-set may be partitioned into two statistically independent subsets, namely:

$$\mathbf{y} = \left[\begin{array}{cc} \mathbf{y}_1^H & \mathbf{y}_2^H \end{array} \right]^H \tag{18}$$

$$\left\{ E \left[\mathbf{y}_1 \mathbf{y}_2^H \right] \right\}_{nm} = 0 \quad \forall \, n, m$$

where $\mathbf{y}_1$ is the stack of $N_1 < N$ SAR images and $\mathbf{y}_2$ is the stack of the remaining $N_2 = N - N_1$ SAR images. By virtue of the statistical independence between the two subsets, no information is available about the differences between any of the phases of the first and the second subsets. This means that the estimation of the interferometric phases may be carried out separately for each subsets, which implies that at most $N_1 - 1 + N_2 - 1 = N - 2$ phases can be retrieved. Extending this argument to the case of N_S independent subsets, it turns out that at most $N - N_S$ phases can be retrieved, corresponding to $rank\,(\mathbf{X}) \leq N - N_S$. Conversely, if the data cannot be partitioned into two subsets, then it means that there are at least $N - 1$ interferometric pairs with a non null coherence. As a consequence, at least $N - 1$ phase differences can be measured. Since the data cannot be partitioned, each of the interferometric phases, φ_n, has to appear in at least one of such $N - 1$ phase differences. Therefore, the ensemble of the $N - 1$ phase difference forms a system of $N - 1$ independent equations, resulting in the possibility to retrieve exactly $N - 1$ interferometric phases. Applying this argument to each subset, one gets that:

$$rank\,(\mathbf{X}) = N - N_S \tag{19}$$

where N is the number of images and N_S is the maximum number of subsets in which the data can be partitioned.

4.1.2 Prior Information Matrix
Under the hypothesis of normally distributed APSs, the computation of the lower right block of the matrix $\mathbf{I}_\alpha$ proceeds directly from (12). In this case, it is readily found that:

$$\mathbf{I}_\alpha = \left[\begin{array}{cc} \mathbf{0} & \mathbf{0} \\ \mathbf{0} & \mathbf{R}_\alpha^{-1} \end{array} \right] \tag{20}$$

where $\mathbf{R}_\alpha$ is the covariance matrix of the APSs.

4.1.3 HCRB
From (17), $\mathbf{X}$ does not depend on $\boldsymbol{\alpha}$, and thus $E_\alpha\,[\mathbf{F}] = \mathbf{F}$. Therefore, the hybrid information matrix may be written as

$$\mathbf{J} = \left[\begin{array}{cc} \boldsymbol{\Theta}^T \mathbf{X} \boldsymbol{\Theta} & \boldsymbol{\Theta}^T \mathbf{X} \\ \mathbf{X} \boldsymbol{\Theta} & \mathbf{X} + \sigma_\alpha^{-2} \mathbf{I}_N \end{array} \right]. \tag{21}$$

Now, computing the inverse of $\mathbf{J}$ and extracting the upper left block, the HCRB for the estimate of θ results:

$$E_{\mathbf{y},\boldsymbol{\alpha}} \left[\left(\widehat{\boldsymbol{\theta}} - \boldsymbol{\theta} \right) \left(\widehat{\boldsymbol{\theta}} - \boldsymbol{\theta} \right)^T \right] \geq \tag{22}$$

$$\left(\boldsymbol{\Theta}^T \mathbf{X} \boldsymbol{\Theta} - \boldsymbol{\Theta}^T \mathbf{X} \left(\mathbf{X} + \mathbf{R}_\alpha^{-1} \right)^{-1} \mathbf{X} \boldsymbol{\Theta} \right)^{-1}$$

where it may be shown that the a necessary and sufficient condition for the bound to exist is that the matrix $\boldsymbol{\Theta}^T \mathbf{X} \boldsymbol{\Theta}$ is full rank.

4.2 A physical interpretation

In order to provide physically meaningful insights about the mechanisms which rule the estimate accuracy in SAR interferometry, we find it convenient to recast (22) in the following form:

$$E_{\mathbf{y},\boldsymbol{\alpha}} \left[\left(\widehat{\boldsymbol{\theta}} - \boldsymbol{\theta} \right) \left(\widehat{\boldsymbol{\theta}} - \boldsymbol{\theta} \right)^T \right] \geq \tag{23}$$

$$\lim_{\varepsilon \to 0} \left(\boldsymbol{\Theta}^T \left(\mathbf{X}_\varepsilon^{-1} + \mathbf{R}_\alpha \right)^{-1} \boldsymbol{\Theta} \right)^{-1}$$

where $\mathbf{X}_\varepsilon = \mathbf{X} + \varepsilon \mathbf{I}_N$ is a perturbation of $\mathbf{X}$. After some matrix manipulations and under the condition that $\boldsymbol{\Theta}^T \mathbf{X} \boldsymbol{\Theta}$ is full rank, it may be proved that (22) and (23) provide the same, finite, bound as $\varepsilon \to 0$. By definition, the matrix $\mathbf{X}$ represents the information that is available about the interferometric phases in dependence of target decorrelation. For this reason, it is natural to associate the inverse of its perturbation, $\mathbf{X}_\varepsilon$, to the covariance matrix of the phase noise due to target decorrelation. Notice that, although such matrix diverges as $\varepsilon \to 0$, if the condition that $\boldsymbol{\Theta}^T \mathbf{X} \boldsymbol{\Theta}$ is full rank is fulfilled the bound in (23) exists finite, and thus the interpretation of $\mathbf{X}_\varepsilon^{-1}$ as a covariance matrix can be retained. After model (3), the presence of the APSs results in a further phase noise, independent of target decorrelation, whose covariance matrix is given by $\mathbf{R}_\alpha$. Hence, the kernel $\left(\mathbf{X}_\varepsilon^{-1} + \mathbf{R}_\alpha \right)$ in (23) represents the covariance matrix of the total phase noise, due to both target decorrelation and the APSs. It follows that the term $\left(\mathbf{X}_\varepsilon^{-1} + \mathbf{R}_\alpha \right)^{-1}$ represent the global information about the interferometric phases, and hence $\boldsymbol{\Theta}^T \left(\mathbf{X}_\varepsilon^{-1} + \mathbf{R}_\alpha \right)^{-1} \boldsymbol{\Theta}$ represents the total information about the parameters of interest $\boldsymbol{\theta}$. The practical implications of this interpretation will be discussed in the next chapter.

4.3 On the validity of the HCRB for InSAR applications

To give an intuitive idea of the conditions that must be met for the HCRB to represent a realistic bound, it is again useful to consider separately the roles of $\mathbf{X}_\varepsilon^{-1}$ and $\mathbf{R}_\alpha$ in (23). Assume that the APS can be neglected with respect to the contribution coming from target decorrelation. In this case, the bound for the variance of the LDF predicted by (23) defaults to the standard CRB, since it ignores the statistical component represented by the APSs. In formula:

$$E_{\mathbf{y}} \left[\left(\widehat{\boldsymbol{\theta}} - \boldsymbol{\theta} \right) \left(\widehat{\boldsymbol{\theta}} - \boldsymbol{\theta} \right)^T \right] \geq \left(\boldsymbol{\Theta}^T \mathbf{X} \boldsymbol{\Theta} \right)^{-1} \tag{24}$$

This bound is quite closely approached by maximum-likelihood estimators at sufficiently large signal-to-noise ratios, or when the number of available data is sufficiently large. In the

framework of InSAR, this means that either the correlation coefficients, the number of images, or the estimation window must be large.

On the other hand, when the APS noise dominates with respect to the source decorrelation, the term $\widetilde{\mathbf{X}}^{-1}$ can be ignored, and from (4), the HCRB for $\boldsymbol{\theta}$ is proportional to the variance of the APS:

$$E_{\mathbf{y},\boldsymbol{\alpha}} \left[\left(\widehat{\boldsymbol{\theta}} - \boldsymbol{\theta} \right) \left(\widehat{\boldsymbol{\theta}} - \boldsymbol{\theta} \right)^T \right] \geq \left(\widetilde{\boldsymbol{\Theta}}^T \widetilde{\mathbf{R}}_\alpha^{-1} \widetilde{\boldsymbol{\Theta}} \right)^{-1} \tag{25}$$

Attention must be paid prior to retaining this result. The role of the variance of the APSs in the estimation process may be described through a threshold like behavior. The fact that this aspect is not handled by the HCRB is an intrinsic limitation of the method, whereas other bounds have been proposed in literature that account properly for threshold effects (27). Practical conditions for retaining the validity of the results will be provided in the following.

4.4 Closed form solutions for InSAR

This last section provides a simple and practical example of an application of the proposed bound (23). For simplicity's sake, the LDF is modeled as a LOS subsidence with constant velocity, v, even though an extension of this analysis to a larger set of unknowns is immediate. In this case the set of the unknowns reduces to a single scalar, v, and the phase functions $\psi_n(v)$ are given by:

$$\psi_n(v) = \frac{4\pi}{\lambda} n\delta t \cdot v \tag{26}$$

δt being the time interval between two nearby acquisitions and λ the wavelength.

To properly characterize the source statistics, we assume that γ_{nm} is determined by an exponential temporal decorrelation (22), plus a thermal noise, uncorrelated from one acquisition to the other:

$$\gamma_{nm} = \gamma_0 \rho^{|n-m|\delta t} + (1 - \gamma_0) \delta_{n-m} \tag{27}$$

where ρ is a parameter describing temporal decorrelation and γ_0 is related to the signal-to-noise ratio via

$$\gamma_0 = \frac{SNR}{1 + SNR}.$$

Finally, let N denote the number of available images and L the number of independent looks within the estimation window.

From the decorrelation model (27), the HCRB for the estimate of the subsidence velocity is easily computed through (17) and (23); see the left panel of Fig. (2). However, to achieve deeper insight on how temporal decorrelation, thermal noise, and APSs impact the accuracy of the estimate, it is convenient to analyze these phenomena separately.

4.4.1 Temporal decorrelation

Neglecting the contribution of thermal noise, the decorrelation model (27) reduces to $\gamma_{nm} = \rho^{|n-m|\delta t}$, for which the matrix $\boldsymbol{\Gamma}^{-1}$ is tridiagonal and computable in a closed form. Neglecting also the contribution of the APSs, from (17) and (23), and after some matrix manipulations it is possible to obtain:

$$\sigma_v^2 = \left(\frac{\lambda}{4\pi\delta t} \right)^2 \frac{1 - \rho^{2\delta t}}{2L\rho^{2\delta t}} \frac{1}{N-1} \stackrel{def}{=} \frac{\sigma_{temp}^2}{N-1} \tag{28}$$

which shows that, in absence of thermal noise and APS, temporal decorrelation acts in such a way as to pose the problem of the estimate of velocity as the estimate of the mean of a normal white process with variance σ_{temp}^2.

4.4.2 Thermal noise and APS

The thermal noise and APS corresponds to the case of **the long-term coherent target**, the same assumption of the Persistent Scatterer (PS), however here we generalize to the case when the scatterer is made by N pixels. By neglecting the temporal decorrelation is neglected, the model (27) becomes $\gamma_{nm} = \gamma_0 + (1 - \gamma_0)\,\delta_{n-m}$, for which the matrix $\mathbf{\Gamma}^{-1}$ is again achievable in a closed form. The computation of $\mathbf{X}$, through (17), leads to:

$$\mathbf{X} = \frac{2L\gamma_0^2}{(1 - \gamma_0)\,(1 + (N - 1)\,\gamma_0)}\left(N \cdot \mathbf{I}_N - \mathbf{1}_N\mathbf{1}_N^T\right) \tag{29}$$

where $\mathbf{1}_N$ denotes the vector in $\mathbb{R}^N$ for which all elements are equal to 1. It is easy to see that the null space of $\mathbf{X}$ is the one dimensional subspace spanned by $\mathbf{1}_N$, therefore $rank\,(\mathbf{X}) = N - 1$. It is then convenient to define an $N - 1 \times N$ phase transformation matrix $\mathbf{D}$ such that the transformed phases are given by the differences of the interferometric phases with respect to a common reference, in formula:

$$\widetilde{\boldsymbol{\varphi}} = \mathbf{D}\boldsymbol{\varphi} \quad \text{such that} \tag{30}$$
$$\widetilde{\varphi}_n = \varphi_n - \varphi_0 \quad \forall\ n = 1, 2...N - 1$$

The covariance matrix for the transformed phases, $\widetilde{\boldsymbol{\varphi}}$, may be readily obtained after (22), yielding:

$$\widetilde{\mathbf{X}}^{-1} = \frac{1 - \gamma_0}{2L\gamma_0^2}\frac{1 + (N - 1)\,\gamma_0}{N}\left(\mathbf{I}_{N-1} + \mathbf{1}_{N-1}\mathbf{1}_{N-1}^T\right) \tag{31}$$
$$\overset{def}{=} \sigma_{noise}^2\left(\mathbf{I}_{N-1} + \mathbf{1}_{N-1}\mathbf{1}_{N-1}^T\right)$$

As for the covariance of the transformed APSs, $\widetilde{\boldsymbol{\alpha}}$, by letting $\mathbf{R}_\alpha = \sigma_\alpha^2\mathbf{I}_N$ it is immediate to see that:

$$E\left[\widetilde{\boldsymbol{\alpha}}\widetilde{\boldsymbol{\alpha}}^T\right] = \widetilde{\mathbf{R}}_\alpha = \mathbf{D}\mathbf{R}_\alpha\mathbf{D}^T = \sigma_\alpha^2\left(\mathbf{I}_{N-1} + \mathbf{1}_{N-1}\mathbf{1}_{N-1}^T\right) \tag{32}$$

Therefore $\widetilde{\mathbf{R}}_\alpha$ has exactly the same structure as (31), from which it follows the important result that, besides a scale factor, thermal noise and APSs affect the estimate accuracy in the same way.

Finally, from (23), the accuracy on the estimate of the subsidence rate is given by:

$$\sigma_v^2 = \left(\frac{\lambda}{4\pi\delta t}\right)^2\frac{12}{N^3 - N}\left(\sigma_\alpha^2 + \sigma_{noise}^2\right) \tag{33}$$

which is analogous to the CRB for a linear regression in presence of a normal white process with variance $\sigma_\alpha^2 + \sigma_{noise}^2$.

4.4.3 Temporal decorrelation plus thermal noise and APSs

At this point, the behavior of the HCRB curve may be qualitatively explained as a mixture of (33) and (28). When the number of images is large, the $1/(N - 1)$ mechanism is dominant; thus, the HCRB may be assumed to be given by (28). On the other hand, when N is small, the dominant contribution is given by thermal noise and APSs, and thus we expect the curve to
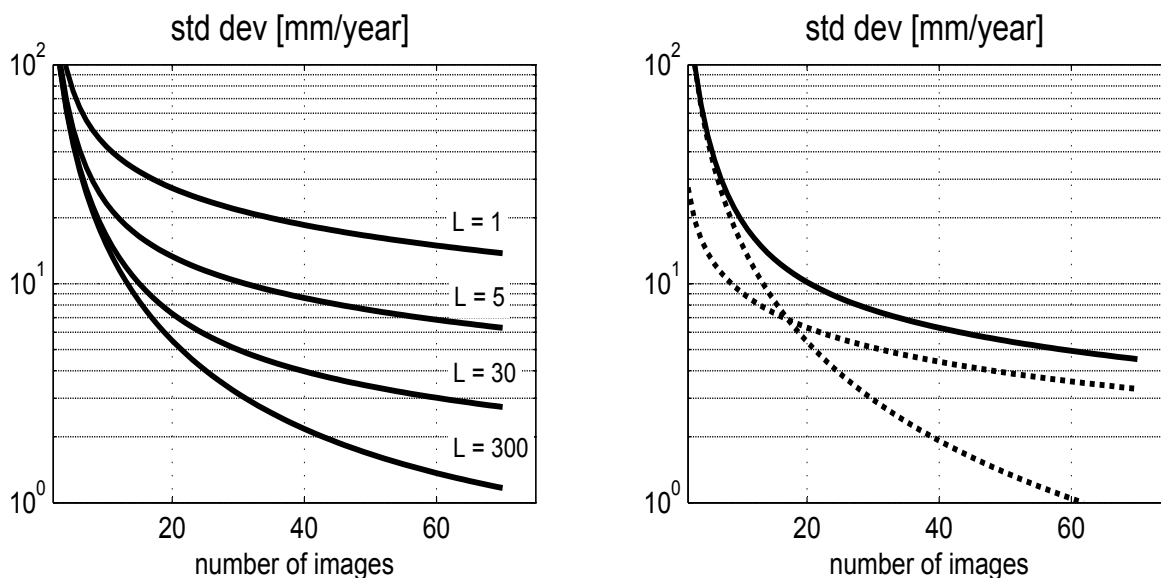
Fig. 2. HCRB for the standard deviation of the estimate of the subsidence velocity. The parameters of this scenario are: $\lambda = 56 \; mm$, $\gamma_0 = 0.7$, $\rho = 0.975$, $\sigma_\alpha = 1$ rad, and $\delta t = 12$ days. The value of ρ was determined according to the work of (13). Left: standard deviation curves obtained corresponding to a number of pixels L equal to $1, 5, 30$, and 300. Right: comparison between the HCRB (continuous line) and the approximations derived in (28) and (35) (dashed lines) for $L = 10$ pixels.

be proportional to $1/\left(N^3 - N\right)$. To find the proportionality factor it suffices to compute the variance for $N = 2$ images. In this case, $\mathbf{X}$ becomes a scalar, and the result is immediate:

$$\sigma_v^2\left(2\right) = \left(\frac{\lambda}{4\pi\delta t}\right)^2 \left(2\sigma_\alpha^2 + \frac{1 - \gamma_0^2 \rho^{2\delta t}}{2\gamma_0^2 \rho^{2\delta t} L}\right) \tag{34}$$

and thus

$$\sigma_v^2\left(N\right) = \sigma_v^2\left(2\right)\frac{6}{N^3 - N} \quad \textit{for N small} \tag{35}$$

The standard deviation of the LDF is plotted in Fig. 2 (left) as a function of the number of images and for different number of pixels, L. The GMES-Sentinel-1 case was assumed, with a repeat pass interval of 12 days, a temporal decorrelation constant of 40 days, a coherence $\gamma_0 = 0.7$ and an APS standard deviation of 1 rad. The two asymptotic behaviors of the LDF standard deviation, corresponding to the PS, $\sigma_v \propto N^{-3/2}$ and to the pure thermal decorrelation, $N^{-1/2}$, are shown on the right.

The value of N where the HCRB curve changes its behavior is determined by intersecting (28) and (35), yielding

$$\widetilde{N} \simeq \sqrt{6\frac{\sigma_v^2\left(2\right)}{\sigma_{temp}^2}} \tag{36}$$

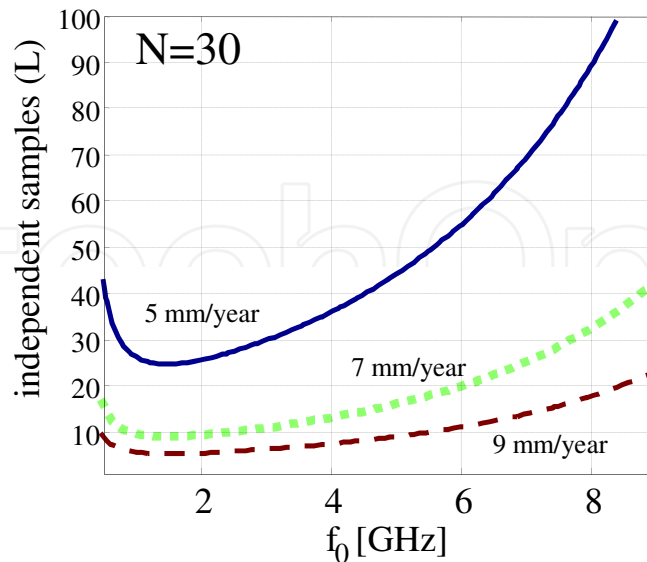This value corresponds to the intersection of the dashed lines in Fig. 2.

Fig. 3. Number of independent samples to be exploited for each target to get a standard deviation of the estimate of the subsidence velocity of 5-7-9 mm/year. Frequencies from L to X band have been exploited.

As a further example, the HCRB allowed us to compute the performances at different frequencies. The number of independent samples to be used to get $\sigma_v = 5, 7$ and 9 mm/year is plotted in Fig. (3).In computing the HCRB, the temporal decorrelation constant has been updated with the square of the wavelength according to the Markov model in (13), and the APS phase standard deviation has been updated inversely to the wavelength, the APS delay being frequency-independent. As a result, the performances drops at the lower frequencies (the L band), due to the scarce sensitivity of phase to displacements, hence the poor SNR. Likewise, there is a drop at the high frequencies due to both the temporal and the APS noises. However, the behavior is flat in the frequencies between S and C band.

4.4.4 Single baseline interferometry

In case of single baseline interferometry, N=2 and there is no way to distinguish between temporal decorrelation and long term stability. Moreover the phase to be estimated is now a scalar. Expression (29) leads to the well known CRB (15):

$$\sigma_\phi^2 = \frac{1 - \gamma^2}{2L\gamma^2}$$

4.5 Conclusions

In this chapter a bound for the parametric estimation of the LDF through InSAR has been discussed. This bound was derived by formulating the problem in such a way as to be handled by the HCRB. This methodology allows for a unified treatment of source decorrelation (target changes, thermal noise, volumetric effect, etc.) and APS under a consistent statistical approach. By introducing some reasonable assumptions, we could obtain some closed form

solutions of practical use in InSAR applications. These solutions provide a quick performance assessment of an InSAR system as a function of its configuration (wavelength, resolution, SNR), the intrinsic scene decorrelation, and the APS variance. Although some limitations may arise at higher wavelengths, due to phase wrapping, the result may still be useful for the design and tuning of the overall system.

5. Phase Linking

The scope of this section is to introduce an algorithm to estimate the set of the interferometric phases, φ_n, comprehensive of the APS contribution. As discussed in previous chapter, assuming such model is equivalent to retaining phase triangularity, namely $\varphi_{nm} = \varphi_n - \varphi_m$. In other words, we are forcing the problem to be structured in such a way as to explain the phases of the data covariance matrix simply through $N - 1$ real numbers, instead than $N(N - 1)/2$. For this reason, the estimated phases will be referred to as Linked Phases, meaning that these terms are the result of the joint processing of all the $N(N - 1)/2$ interferograms. Accordingly, the algorithm to be described in this section will be referred to as Phase Linking (PL).

An overview of the algorithm is given in the block diagram of Fig. 4. The algorithm is made of two steps, the first is the phase linking, where the set of N linked phases are optimally estimated by exploiting the $N(N - 1)/2$ interferograms. These phases corresponds to the optical path, hence at a second step, the APS, the DEM (the target heights) and the deformation parameters are retrieved.
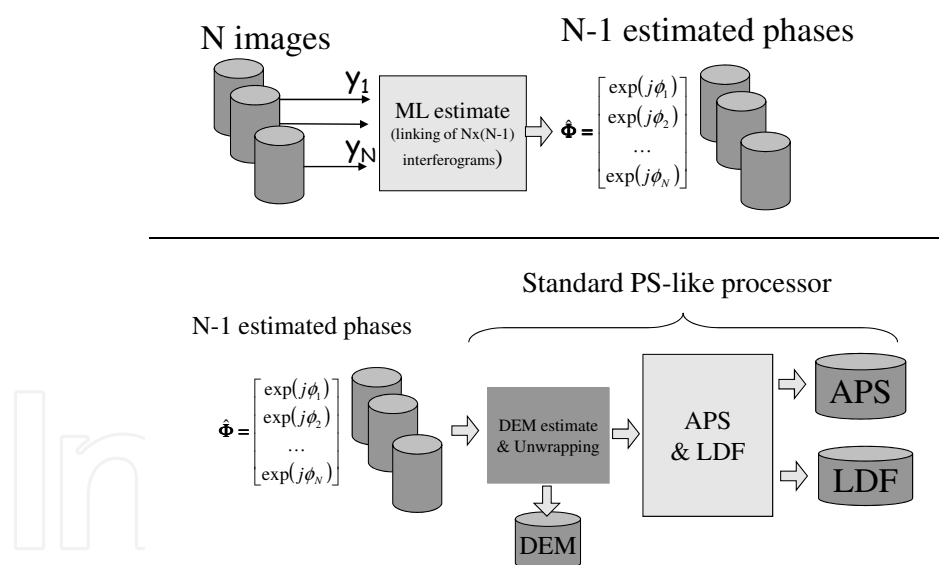

Fig. 4. Block diagram of the two step algorithm for estimating topography and subsidences.

Before going into details, it is important to note that phase triangularity is automatically satisfied if the data covariance matrix is estimated through a single sample of the data, since $\angle(y_n y_m^*) = \angle(y_n) - \angle(y_m)$. It follows that a necessary condition for the PL algorithm to be effective is that a suitable estimation window is exploited.

Since the interferometric phases affect the data covariance matrix only through their differences, one phase (say, $n = 0$) will be conventionally used as the reference, in such a way

as to estimate the $N - 1$ phase differences with respect to such reference. Notice that this is equivalent to estimating N phases under the constraint that $\varphi_0 = 0$. Therefore, not to add any further notation, in the following the $N - 1$ phase differences will be denoted through $\{\varphi_n\}_1^{N-1}$. From (7), the log-likelihood function (times -1) is proportional to:

$$f\left(\varphi_1, ..\varphi_{N-1}\right) \quad \propto \quad \sum_{l=1}^{L} \mathbf{y}^H\left(r_l, x_l\right) \phi \mathbf{\Gamma}^{-1} \phi^H \mathbf{y}\left(r_l, x_l\right) \tag{37}$$

$$\propto \quad trace\left(\phi \mathbf{\Gamma}^{-1} \phi^H \widehat{\mathbf{R}}\right)$$

where $\widehat{\mathbf{R}}$ is the sample estimate of $\mathbf{R}$ or, in other words, it is the matrix of all the available interferograms averaged over Ω. Rewriting (37), it turns out that the log-likelihood function may be posed as the following form:

$$f\left(\varphi_1, ..\varphi_{N-1}\right) \propto \xi^H\left(\mathbf{\Gamma}^{-1} \circ \widehat{\mathbf{R}}\right) \xi \tag{38}$$

where $\xi^H = \begin{bmatrix} 1 & \exp\left(j\varphi_1\right) & ... & \exp\left(j\varphi_{N-1}\right) \end{bmatrix}$. Hence, the ML estimation of the phases $\{\varphi_n\}_1^{N-1}$ is equivalent to the minimization of the quadratic form of the matrix $\mathbf{\Gamma}^{-1} \circ \widehat{\mathbf{R}}$ under the constraint that ξ is a vector of complex exponentials. Unfortunately, we could not find any closed form solution to this problem, and thus we resorted to an iterative minimization with respect to each phase, which can be done quite efficiently in closed form:

$$\widehat{\varphi}_p^{(k)} = \angle\left\{ \sum_{n \neq p}^{N} \left\{\mathbf{\Gamma}^{-1}\right\}_{np} \left\{\widehat{\mathbf{R}}\right\}_{np} \exp\left(j\widehat{\varphi}_n^{(k-1)}\right) \right\} \tag{39}$$

where k is the iteration step. The starting point of the iteration was assumed as the phase of the vector minimizing the quadratic form in (38) under the constraint $\xi_0 = 1$.

Figures (5 - 7) show the behavior of the variance of the estimates of the $N - 1$ phases $\{\varphi_n\}_1^{N-1}$ achieved by running Monte-Carlo simulations with three different scenarios, represented by the matrices $\mathbf{\Gamma}$. In order to prove the effectiveness of the PL algorithm, we considered two phase estimators commonly used in literature. The trivial solution, consisting in evaluating the phase of the corresponding L-pixel averaged interferograms formed with respect to the first ($n = 0$) image, namely

$$\widehat{\varphi}_n = \angle\left(\left\{\widehat{\mathbf{R}}\right\}_{0n}\right) \tag{40}$$

is named PS-like. The estimator referred to as AR(1) is obtained by evaluating the phases of the interferograms formed by consecutive acquisitions (i.e. n and $n - 1$) and integrating the result. In formula:

$$\widehat{\zeta}_n = \angle\left(\left\{\widehat{\mathbf{R}}\right\}_{n,n-1}\right); \quad \widehat{\varphi}_n = \sum_{k=1}^{n} \widehat{\zeta}_n \tag{41}$$

The name AR(1) was chosen for this phase estimator because it yields the global minimizer of (38) in the case where the sources decorrelate as an AR(1) process, namely $\gamma_{nm} = \rho^{|n-m|}$, where $\rho \in (0, 1)$. This statement may be easily proved by noticing that if $\{\mathbf{\Gamma}\}_{nm} = \rho^{|n-m|}$, then $\mathbf{\Gamma}^{-1}$ is tridiagonal, and thus $\widehat{\zeta}_n$, in (41), represents the optimal estimator of the phase difference $\varphi_n - \varphi_{n-1}$. In literature this solution has been applied to compensate for temporal decorrelation in (7), (8), (6), even though in all of these works such choice was made after heuristical considerations. Finally, the CRB for the phase estimates has been computed by

zeroing the variance of the APSs. In all the simulations it has been exploited an estimation window as large as 5 independent samples.

In Fig. (5) it has been assumed a coherence matrix determined by exponential decorrelation. As stated above, in this case the AR(1) estimator yields the global minimizers of (38), and so does the PL algorithm, which defaults to this simple solution. The PS-like estimator, instead, yields significantly worse estimates, due to the progressive loss of coherence induced by the exponential decorrelation. In Fig. (6) it is considered the case of a constant decorrelation throughout all of the interferograms. The result provided by the AR(1) estimator is clearly unacceptable, due to the propagation of the errors caused by the integration step. Conversely, both the PS-like and the PL estimators produce a stationary phase noise, which is consistent with the kind of decorrelation used for this simulation. Furthermore, it is interesting to note that the Linked Phases are less dispersed, proving the effectiveness of the algorithm also in this simple scenario. Finally, a complex scenario is simulated in Fig. (7) by randomly choosing the coherence matrix, under the sole constraints that $\{\mathbf{\Gamma}\}_{nm} > 0 \ \forall \ n, m$ and that $\mathbf{\Gamma}$ is positive definite. As expected, none of the AR(1) and the PS-like estimators is able to handle this scenario properly, either due to error propagation and coherence losses. In this case, only through the joint processing of all the interferograms it is possible to retrieve reliable phase estimates.
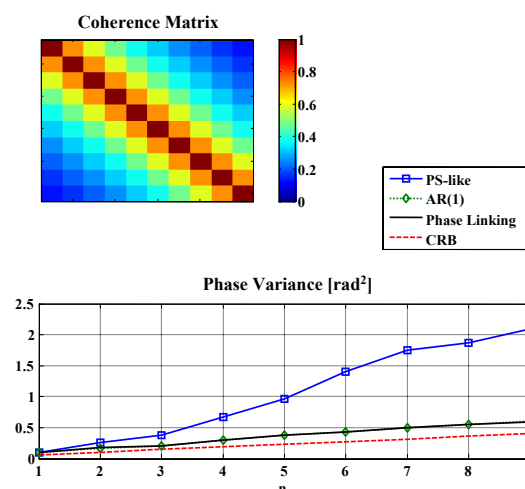

Fig. 5. Variance of the phase estimates. Coherence model: $\{\mathbf{\Gamma}\}_{nm} = \rho^{|n-m|}; \rho = 0.8$.

5.1 Phase unwrapping

As stated above, the splitting of the MLE into two steps is advantageous provided that the two resulting sub-problems are actually easier to solve than the original problem. Despite we could not find a closed form solution to the PL problem, it must be highlighted that the algorithm does not require the exploration of the parameter space, thus granting an interesting computational advantage over the one step MLE, especially in the case of a complex initial parametrization. Instead, difficulties may arise when dealing with the estimation of the original parameters from the linked phases, since the PL algorithm does not solve for the 2π ambiguity. As a consequence, a Phase Unwrapping (PU) step is required prior to the moving to the estimation of the parameters of interest. However, the discussion of a PU technique is out of the scope of this chapter, we just observe that, once a set of liked phases phases $\widehat{\varphi}_n$ has
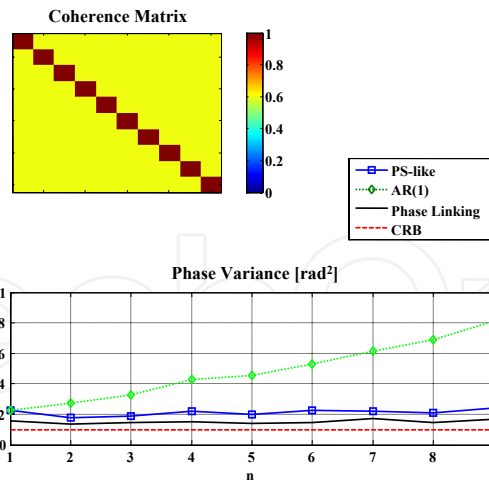
Fig. 6. Variance of the phase estimates. Coherence model: $\{\mathbf{\Gamma}\}_{nm} = \gamma_0 + (1 - \gamma_0)\,\delta_{n-m}$; $\gamma_0 = 0.6$.

been estimated, we just approach PU as in conventional PS processing, that is quite simple and well tested (1), (5).

6. Parameter estimation

Once the 2π ambiguity has been solved, the linked phases may be expressed in a simple fashion by modifying the phase model in (3) in such a way as to include the estimate error committed in the first step. In formula:

$$\widehat{\boldsymbol{\varphi}} = \boldsymbol{\psi}\left(\boldsymbol{\theta}\right) + \boldsymbol{\alpha} + \boldsymbol{v} \tag{42}$$

where $\boldsymbol{v}$ represents the estimate error committed by the PL algorithm or, in other words, the phase noise due to target decorrelation. After the properties of the MLE, $\boldsymbol{v}$ is asymptotically distributed as a zero-mean multivariate normal process, with the same covariance matrix as the one predicted by the CRB (30). In the case of InSAR, the term "asymptotically" is to be understood to mean that either the estimation window is large or there is a sufficient number of high coherence interferometric pairs. If these conditions are met, then it sensible to model the pdf of $\boldsymbol{v}$ as:

$$\boldsymbol{v} \sim N\left(\mathbf{0}, \lim_{\varepsilon \to 0}\left(\mathbf{X} + \varepsilon\mathbf{I}_N\right)^{-1}\right) \tag{43}$$

where the covariance matrix of $\boldsymbol{v}$ has been determined after (23), by zeroing the contribution of the APSs. Notice that the limit operation could be easily removed by considering a proper transformation of the linked phases in (42), as discussed in section 4.2. Nevertheless, we regard that dealing with non transformed phases provides a more natural exposition of how parameter estimation is performed, and thus we will retain the phase model in (42).

After the discussion in the previous chapter, the APS may be modeled as a zero-mean stochastic process, highly correlated over space, uncorrelated from one acquisition to the other and, as a first approximation, normally distributed. This leads to expressing the pdf of the linked phases in as

$$\widehat{\boldsymbol{\varphi}} \sim N\left(\boldsymbol{\psi}\left(\boldsymbol{\theta}\right), \lim_{\varepsilon \to 0}\left(\mathbf{W}_\varepsilon\right)\right)$$
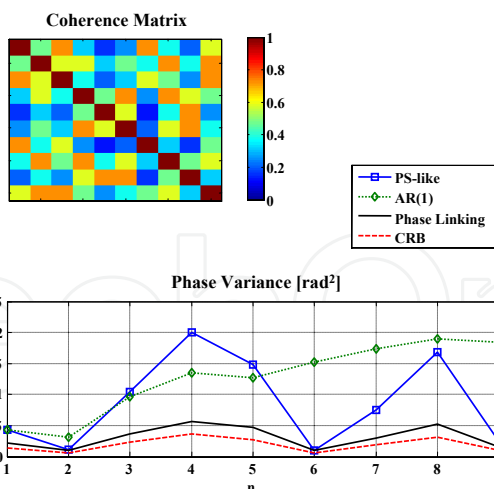
Fig. 7. Variance of the phase estimates. Coherence model: random.

where $\mathbf{W}_\varepsilon$ is the covariance matrix of the total phase noise,

$$\mathbf{W}_\varepsilon = (\mathbf{X} + \varepsilon \mathbf{I}_N)^{-1} + \sigma_\alpha^2 \mathbf{I}_N, \tag{44}$$

and σ_α^2 is the variance of the APS.

In order to provide a closed form solution for the estimation of $\boldsymbol{\theta}$ from the linked phase, $\widehat{\boldsymbol{\varphi}}$, we will focus on the case where the relation between the terms $\boldsymbol{\psi}(\boldsymbol{\theta})$ and $\boldsymbol{\theta}$ is linear, namely $\boldsymbol{\psi}(\boldsymbol{\theta}) = \boldsymbol{\Theta}\boldsymbol{\theta}$. This passage does not involve any loss of generality, as long as that $\boldsymbol{\theta}$ is interpreted as the set of weights which represent $\boldsymbol{\psi}(\boldsymbol{\theta})$ in some basis (such as a polynomial basis). At this point, the MLE of $\boldsymbol{\theta}$ from $\widehat{\boldsymbol{\varphi}}$ may be easily derived by minimizing with respect to $\boldsymbol{\theta}$ the quadratic form:

$$(\widehat{\boldsymbol{\varphi}} - \boldsymbol{\Theta}\boldsymbol{\theta})^T \mathbf{W}_\varepsilon^{-1} (\widehat{\boldsymbol{\varphi}} - \boldsymbol{\Theta}\boldsymbol{\theta}), \tag{45}$$

which yields the linear estimator

$$\widehat{\boldsymbol{\theta}} = \mathbf{Q}\widehat{\boldsymbol{\varphi}}, \tag{46}$$

where

$$\mathbf{Q} = \lim_{\varepsilon \to 0} \left(\boldsymbol{\Theta}^T \mathbf{W}_\varepsilon^{-1} \boldsymbol{\Theta} \right)^{-1} \boldsymbol{\Theta}^T \mathbf{W}_\varepsilon^{-1} \tag{47}$$

Therefore, the MLE of $\boldsymbol{\theta}$ from $\widehat{\boldsymbol{\varphi}}$ is implemented through a weighted L2 norm fit of the model $\boldsymbol{\psi}(\boldsymbol{\theta}) = \boldsymbol{\Theta}\boldsymbol{\theta}$, and $\mathbf{W}_\varepsilon^{-1}$ may be interpreted as the set of weights which allows to fit the model accounting for target decorrelation and the APSs. It can be shown that the condition that $\boldsymbol{\Theta}^T \mathbf{X} \boldsymbol{\Theta}$ is full rank is sufficient to ensure the finiteness of the matrix $\mathbf{Q}$.

By plugging (47) into (46) it turns out that $\widehat{\boldsymbol{\theta}}$ is an unbiased estimator of $\boldsymbol{\theta}$ and that the covariance matrix of the estimates is given by:

$$E\left[\left(\widehat{\boldsymbol{\theta}} - \boldsymbol{\theta} \right) \left(\widehat{\boldsymbol{\theta}} - \boldsymbol{\theta} \right)^T \right] = \mathbf{Q}\mathbf{W}_\varepsilon \mathbf{Q}^T \tag{48}$$

$$= \lim_{\varepsilon \to 0} \left(\boldsymbol{\Theta}^T \left((\mathbf{X} + \varepsilon \mathbf{I})^{-1} + \sigma_\alpha^2 \mathbf{I} \right)^{-1} \boldsymbol{\Theta} \right)^{-1}$$

which is the same as (23). The equivalence between (23) and (48) shows that the two step procedure herein described is asymptotically consistent with the HCRB, and thus it may be regarded as an optimal solution at sufficiently large signal-to-noise ratios, or when the data space is large.

It is important to note that the peculiarity of the phase model (42), on which parameter estimation has been based, is constituted by the inclusion of phase noise due to target decorrelation, represented by v. In the case where this term is dominated by the APS noise, model (42) would tends to default to the standard model exploited in PS processing. Accordingly, in this case the weighted fit carried out by (47) substantially provides the same results as an unweighted fit. In the framework of InSAR, this is the case where the LDF is to be investigated over distances larger than the spatial correlation length of the APS. Therefore, the usage of a proper weighting matrix $\mathbf{W}_\varepsilon^{-1}$ is expected to prove its effectiveness in cases where not only the average displacement of an area is under analysis, but also the local strains.

7. Conditions for the validity of the HCRB for InSAR applications

The equivalence between (23) and (48) provides an alternative methodology to compute the lower bounds for InSAR performance, through which it is possible to achieve further insights on the mechanisms that rule the InSAR estimate accuracy. In particular, (48) has been derived under two hypotheses:

1. the accuracy of the linked phases is close to the CRB;
2. the linked phases can be correctly unwrapped.

As previously discussed, the condition for the validity of hypothesis 1) is that either the estimation window is large or there is a sufficient number of high coherence interferometric pairs. Approximately, this hypothesis may be considered valid provided that the CRB standard deviation of each of the linked phases is much lower than π. Provided that hypothesis 1) is satisfied, a correct phase unwrapping can be performed provided that both the displacement field and the APSs are sufficiently smooth functions of the slant range, azimuth coordinates (15), (31). Accordingly, as far as InSAR applications are concerned, the results predicted by the HCRB in are meaningful as long as phase unwrapping is not a concern.

8. An experiment on real data

This section is reports an example of application of the two step MLE so far developed. The data-set available is given by 18 SAR images acquired by ENVISAT[1] over a 4.5×4 Km^2 (slant range, azimuth) area near Las Vegas, US. The scene is characterized by elevations up 600 meters and strong lay-over areas. The normal and temporal baseline spans are about 1400 meters and 912 days, respectively. The scene is supposed to exhibit a high temporal stability. Therefore, both temporal decorrelation and the LDF are expected to be negligible. However, many image pairs are affected by a severe baseline decorrelation. Fig. (8) shows the interferometric coherence for three image pairs, computed after removing the topographical contributions to the phase. The first and the third panels (high normal baseline) are characterized by very low coherence values throughout the whole scene, but for areas in backslope, corresponding to the bottom right portion of each panel. These panels fully confirm the hypothesis that the scene

---

[1] The SAR sensor aboard ENVISAT operates in C-Band ($\lambda = 5.6\ cm$) with a resolution of about $9 \times 6\ m^2$ (slant range - azimuth) in the Image mode.
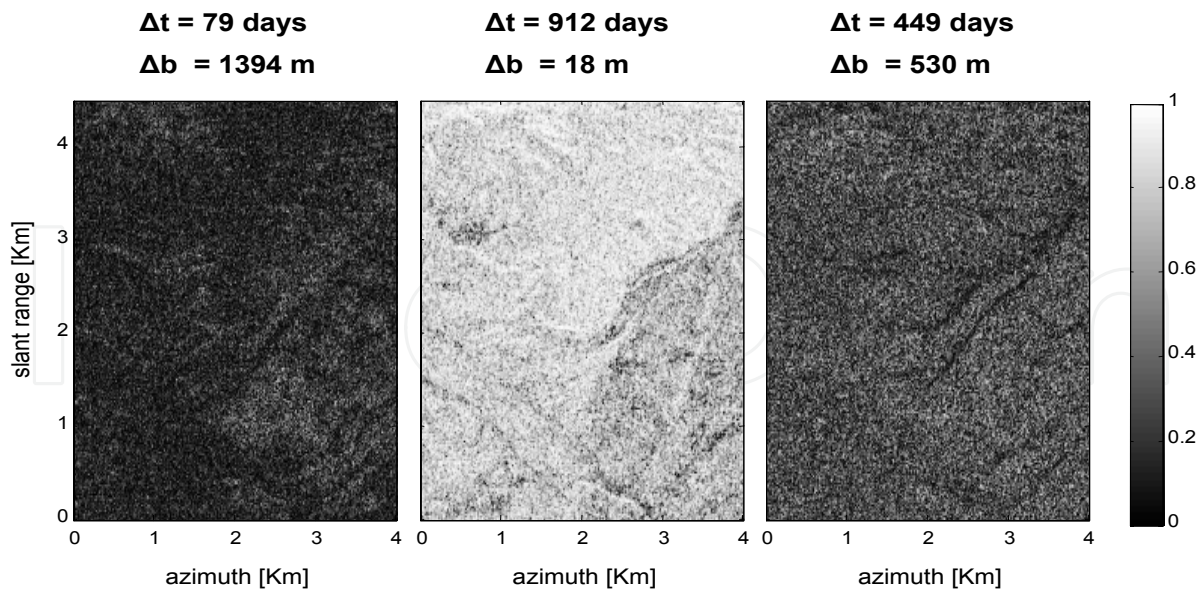
Fig. 8. Scene coherence computed for three image pairs. The coherences have been computed by exploiting a 3×9 pixel window. The topographical contributions to phase have been compensated for by exploiting the estimated DEM.

is to be characterized as being constituted by distributed targets, affected by spatial decorrelation. On the other side, the high coherence values in the middle panel (low normal baseline, high temporal baseline) confirms the hypothesis of a high temporal stability. The aim of this section is to show the effectiveness of the two step MLE previously depicted by performing a pixel by pixel estimation of the local topography and the LDF, accounting for the target decorrelation affecting the data. There are two reasons why the choice of such a data-set is suited to this goal:

- an a priori information about target statistics, represented by the matrix $\mathbf{\Gamma}$, is easily available by using an SRTM DEM;
- the absence of a relevant LDF in the imaged scene represents the best condition to assess the accuracy.

8.1 Phase Linking and topography estimation

Prior to running the PL algorithm, each SAR image have been demodulated by the interferometric phase due to topographic contributions, computed by exploiting the SRTM DEM. In order to avoid problems due to spectral aliasing, each image have been oversampled by a factor 2 in both the slant range and the azimuth directions. Then the sample covariance matrix has been computed by averaging all the interferograms over the estimation window, namely:

$$\left\{ \widehat{\mathbf{R}} \right\}_{nm} = \mathbf{y}_n^H \mathbf{y}_m \tag{49}$$

where $\mathbf{y}_n$ is a vector corresponding to the pixels of the $n - th$ image within the estimation window. The size of the estimation window has been fixed in 3×9 pixels (slant range, azimuth), corresponding to about 5 independent samples and an imaged area as large as 12×20 m^2 in the slant range, azimuth plane.

The PL algorithm has been implemented as shown by equations (38), (39), where the matrix $\mathbf{\Gamma}$ has been computed at every slant range, azimuth location as a linear combination between the sample estimate within the estimation window and the a priori information provided by the SRTM DEM. Then, all the interferograms have been normalized in amplitude, flattened by the linked phases, and added up, in such a way as to define an index to assess the phase stability at each slant range, azimuth location. In formula:

$$\mathrm{Y} = \sum_{nm} \frac{\mathbf{y}_n^H \mathbf{y}_m}{\|\mathbf{y}_n\| \, \|\mathbf{y}_m\|} \exp\left(j\left(\widehat{\varphi}_m - \widehat{\varphi}_n\right)\right) \tag{50}$$

The precise topography has been estimated by plugging the phase stability index defined in (50) and the linked phases, $\widehat{\varphi}_n$, into a standard PS processors. More explicitly, the phase stability index has been used as a figure of merit for sampling the phase estimates on a sparse grid of reliable points, to be used for APS estimation and removal. After removal of the APS, the residual topography has been estimated on the full grid by means of a Fourier Transform (1), (5), namely:

$$\widehat{q} = \arg\max_q \left\{ \left| \sum_n \exp\left(j\left(\widehat{\varphi}_n - k_z\left(n\right)q\right)\right) \right| \right\} \tag{51}$$

where $\widehat{q}$ is the topographic error with respect to the SRTM DEM and $k_z\left(n\right)$ is the height to phase conversion factor for the $n - th$ image.

The resulting elevation map shows a remarkable improvement in the planimetric and altimetric resolution, see Fig. (9). In order to test the DEM accuracy, the interferograms for three different image pairs have been formed and compensated for the precise DEM and the APS, as shown in Fig. (10, top row). Notice that the interferograms decorrelate as the baseline increases, but for the areas in backslope. In these areas, it is possible to appreciate that the phases are rather good, showing no relevant residual fringes.

The effectiveness of the Phase Linking algorithm in compensating for spatial decorrelation phenomena is visible in Fig. (10, bottom row), where the three panels represent the phases of the same three interferograms as in the top row obtained by computing the (wrapped) differences among the LPs: $\widehat{\varphi}_{nm} = \widehat{\varphi}_n - \widehat{\varphi}_m$. It may be noticed that the estimated phases exhibit the same fringe patterns as the original interferogram phases, but the phase noise is significantly reduced, whatever the slope.

This is remarked in Fig. 11, where the histogram of the residual phases of the 1394 m interferogram (continuous line) is compared to the histogram of the estimated phases of the same interferogram (dashed line). The width of the central peak may be assessed in about 1 rad, corresponding to a standard deviation of the elevation of about 1 m.

Finally, Fig. 12 reports the error with respect to the SRTM DEM as estimated by the approach depicted above (left) and by a conventional PS analysis (right). More precisely, the result in the right panel has been achieved by substituting the linked phases with the interferogram phases in (51). Note that APS estimation and removal has been based in both cases on the linked phases, in such a way as to eliminate the problem of the PS candidate selection in the PS algorithm. The reason for the discrepancy in the results provided by the Phase Linking and the PS algorithms is that the data is affected by a severe spatial decorrelation, causing the Permanent Scatterer model to break down for a large portion of pixels.
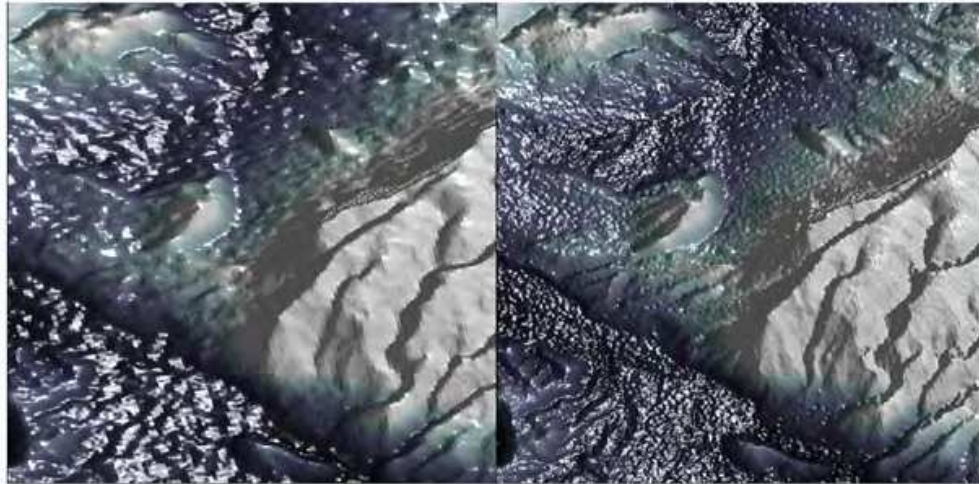
Fig. 9. Absolute height map in slant range - azimuth coordinates. Left: elevation map provided by the SRTM DEM. Right: estimated elevation map

8.2 LDF estimation

A first analysis of the residual fringes (see Fig. 10, middle panels) shows that, as expected, no relevant displacement occurred during the temporal span of 912 days under analysis. This result confirms that the residual phases may be mostly attributed to decorrelation noise and to the residual APSs. Thereafter, all the $N-1$ estimated residual phases have been unwrapped, in order to estimate the LDF as depicted in section 6. For sake of simplicity, we assumed a linear subsidence model for each pixel, that is

$$\Theta = \frac{4\pi}{\lambda} \begin{bmatrix} \Delta t_1 & \Delta t_2 & \cdots & \Delta t_N \end{bmatrix}^T \tag{52}$$

being λ the wavelength and Δt_n the acquisition time of the $n-th$ image with respect to the reference image. The weights of the estimator (47) have been derived from the estimates of Γ, according to (44). As pointed up in section 6, the weighted estimator (47) is expected to prove its effectiveness over a standard fit (in this case, a linear fitting) in the estimation of local scale displacements, for which the major source of phase noise is due to target decorrelation. To this aim, the estimated phases have been selectively high-pass filtered along the slant range, azimuth plane, in such a way as to remove most of the APS contributions and deal only with local deformations.

Figure (13) shows the histograms of the estimated LOS velocities obtained by the weighted estimator (47) and the standard linear fitting. As expected, the scene does not show any relevant subsidence and the weighted estimator achieves a lower dispersion of the estimates than the standard linear fitting. The standard deviation of the estimates of the LOS velocity produced by the weighted estimator (47) may be quantified in about 0.5 $mm/year$, whereas the HCRB standard deviation for the estimate of the LOS velocity is 0.36 $mm/year$, basing on the average scene coherence.

The reliability of the LOS velocity estimates has been assessed by computing the mean square error between the phase history and the fitted model at every slant range, azimuth location, see Fig. (14). It is worth noting that among the points exhibiting high reliability, few also exhibit a velocity value significantly higher that the estimate dispersion.
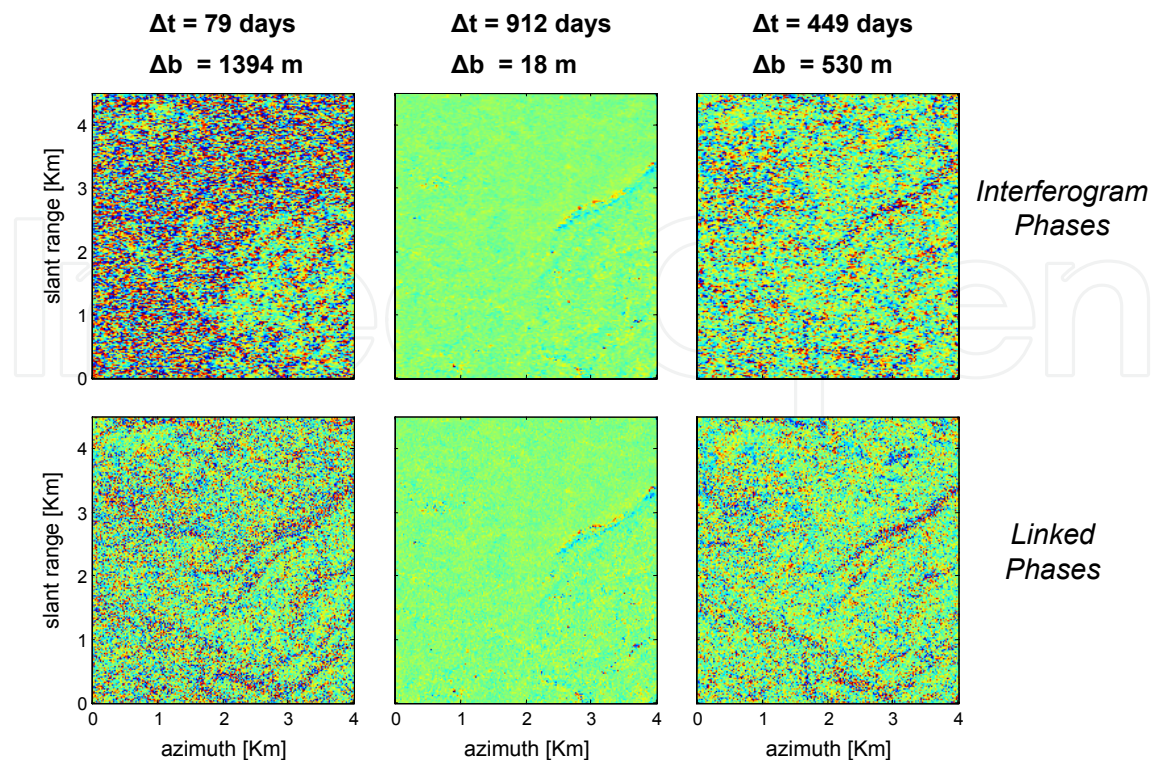
Fig. 10. Top row: wrapped phases of three interferograms after subtracting the estimated topographical and APS contributions. Each panel has been filtered, in order yield the same spatial resolution as the estimated interferometric phases (3 × 9 pixel). Bottom row: wrapped phases of the same three interferograms obtained as the differences of the corresponding LPs, after subtracting the estimated topographical and APS contributions.

9. Conclusions

This section has provided an analysis of the problems that may arise when performing interferometric analysis over scenes characterized by decorrelating scatterers. This analysis has been performed mainly from a statistical point of view, in order to design algorithms yielding the lowest variance of the estimates. The PL algorithm has been proposed as a MLE of the (wrapped) interferometric phases directly from the focused SAR images, capable of com-
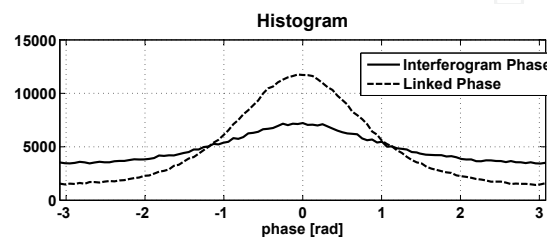
Fig. 11. Histograms of the phase residuals shown in the top and bottom left panels of Fig. 10, corresponding to a normal baseline of 1394 *m*.

**Topography estimated
from the linked phases**

**Topography estimated
according to the PS
processing**
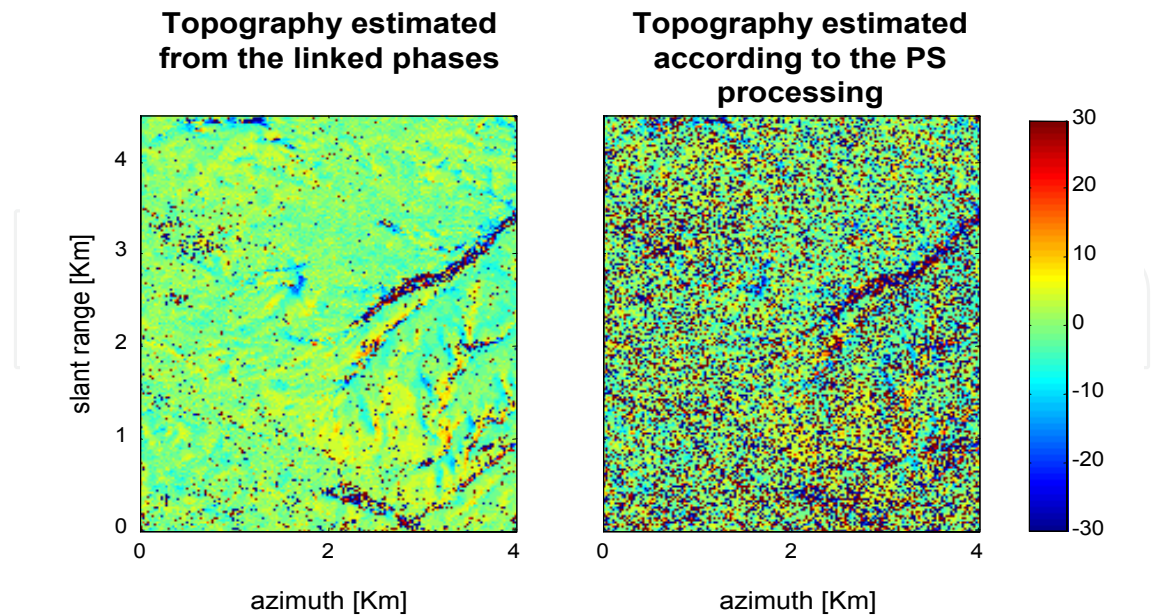
Fig. 12. Left: topography estimated from the linked phases. Right; topography estimated according to the PS processing. The color scale ranges from -30 to 30 meters.
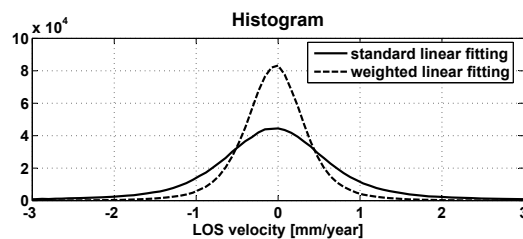

Fig. 13. Histograms of the estimates of the LOS velocity obtained by a standard linear fitting and the weighted estimator (47).

pensating the loss of information due to target decorrelation by combining all the available interferograms. This technique has been proven to be very effective in the case where the target statistics are at least approximately known, getting close to the CRB even for highly decorrelated sources. Basing on the asymptotic properties of the statistics of the phase estimates, a second MLE has been proposed to optimally fit an arbitrary LDF model from the unwrapped estimated phases, taking into account both the phase noise due target decorrelation and the presence of the APSs. The estimates have been to shown to be asymptotically unbiased and minimum variance.

The concepts presented in this chapter have been experimentally tested on an 18 image dataset spanning a temporal interval of about 30 months and a total normal baseline of about 1400 m. As a result, a DEM of the scene has been produced with 12×20 m^2 spatial resolution and an elevation dispersion of about 1 m. The dispersion of the LOS subsidence velocity estimate has been assessed to be about 0.5 $mm/year$.
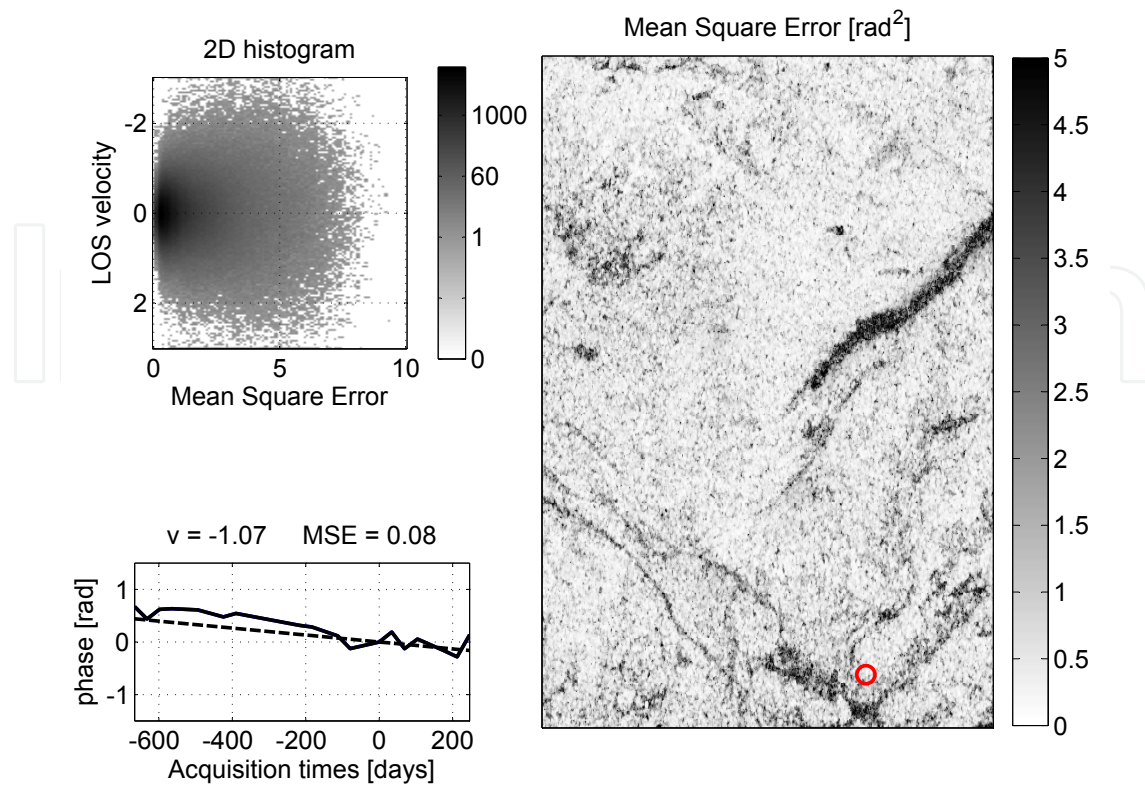
Fig. 14. Right: map of the Mean Square Errors. Top left: 2D histogram of LOS velocities estimated through weighted linear fitting and Mean Square Errors. Bottom left: phase history of a selected point (continuous line) and the correspondent fitted LDF model (dashed line). The location of this point is indicated by a red circle in the right panel.

One critical issue of this approach, common to any ML estimation technique, is the need for a reliable estimate of the scene coherence for every interferometric pair, required to drive the algorithms. In the case where target decorrelation is mainly determined by the target spatial distribution, it has been shown that a viable solution is to exploit the availability of a DEM in order to provide an initial estimate of the coherences. The case where temporal decorrelation is dominant is clearly more critical, due to the intrinsic difficulty in foreseeing the temporal behavior of the targets. Solving this problem requires the exploitation of either a very large estimation window or, which would be better, of a proper physical modeling of temporal decorrelation, accounting for Brownian Motion, seasonality effects, and other phenomena.

10. References

[1] A. Ferretti, C. Prati, and F. Rocca, "Permanent scatterers in SAR interferometry," in *International Geoscience and Remote Sensing Symposium, Hamburg, Germany, 28 June–2 July 1999*, 1999, pp. 1–3.

[2] ——, "Permanent scatterers in SAR interferometry," *IEEE Transactions on Geoscience and Remote Sensing*, vol. 39, no. 1, pp. 8–20, Jan. 2001.

[3] N. Adam, B. M. Kampes, M. Eineder, J. Worawattanamateekul, and M. Kircher, "The development of a scientific permanent scatterer system," in *ISPRS Workshop High Resolution Mapping from Space, Hannover, Germany, 2003*, 2003, p. 6 pp.

[4] C. Werner, U. Wegmuller, T. Strozzi, and A. Wiesmann, "Interferometric point target analysis for deformation mapping," in *International Geoscience and Remote Sensing Symposium, Toulouse, France, 21–25 July 2003*, 2003, pp. 3 pages, cdrom.

[5] A. Ferretti, C. Prati, and F. Rocca, "Nonlinear subsidence rate estimation using permanent scatterers in differential SAR interferometry," *IEEE Transactions on Geoscience and Remote Sensing*, vol. 38, no. 5, pp. 2202–2212, Sep. 2000.

[6] A. Hooper, H. Zebker, P. Segall, and B. Kampes, "A new method for measuring deformation on volcanoes and other non-urban areas using InSAR persistent scatterers," *Geophysical Research Letters*, vol. 31, pp. L23 611, doi:10.1029/2004GL021 737, Dec. 2004.

[7] R. Hanssen, D. Moisseev, and S. Businger, "Resolving the acquisition ambiguity for atmospheric monitoring in multi-pass radar interferometry," in *International Geoscience and Remote Sensing Symposium, Toulouse, France, 21–25 July 2003*, 2003, pp. cdrom, 4 pages.

[8] Y. Fialko, "Interseismic strain accumulation and the earthquake potential on the southern San Andreas fault system," *Nature*, vol. 441, pp. 968–971, Jun. 2006.

[9] P. Berardino, G. Fornaro, R. Lanari, and E. Sansosti, "A new algorithm for surface deformation monitoring based on small baseline differential SAR interferograms," *IEEE Transactions on Geoscience and Remote Sensing*, vol. 40, no. 11, pp. 2375–2383, 2002.

[10] P. Berardino, F. Casu, G. Fornaro, R. Lanari, M. Manunta, M. Manzo, and E. Sansosti, "A quantitative analysis of the SBAS algorithm performance," *International Geoscience and Remote Sensing Symposium, Anchorage, Alaska, 20–24 September 2004*, pp. 3321–3324, 2004.

[11] G. Fornaro, A. Monti Guarnieri, A. Pauciullo, and F. De-Zan, "Maximum liklehood multibaseline sar interferometry," *Radar, Sonar and Navigation, IEE Proceedings -*, vol. 153, no. 3, pp. 279–288, June 2006.

[12] A. Ferretti, F. Novali, D. Z. F, C. Prati, and F. Rocca, "Moving from ps to slowly decorrelating targets: a prospective view,," in *European Conference on Synthetic Aperture Radar, Friedrichshafen, Germany, 2–5 June 2008*, 2008, pp. 1–4.

[13] F. Rocca, "Modeling interferogram stacks," *Geoscience and Remote Sensing, IEEE Transactions on*, vol. 45, no. 10, pp. 3289–3299, Oct. 2007.

[14] A. Monti Guarnieri and S. Tebaldini, "On the exploitation of target statistics for sar interferometry applications," *Geoscience and Remote Sensing, IEEE Transactions on*, vol. 46, no. 11, pp. 3436–3443, Nov. 2008.

[15] R. Bamler and P. Hartl, "Synthetic aperture radar interferometry," *Inverse Problems*, vol. 14, pp. R1–R54, 1998.

[16] G. Franceschetti and G. Fornaro, "Synthetic aperture radar interferometry," in *Synthetic Aperture Radar processing*, G. Franceschetti and R. Lanari, Eds. CRC Press, 1999, ch. 4, pp. 167–223.

[17] P. Rosen, S. Hensley, I. R. Joughin, F. K. Li, S. Madsen, E. Rodríguez, and R. Goldstein, "Synthetic aperture radar interferometry," *Proceedings of the IEEE*, vol. 88, no. 3, pp. 333–382, Mar. 2000.

[18] A. Ferretti, A. Monti Guarnieri, C. Prati, F. Rocca, and D. Massonnet, *InSAR Principles: Guidelines for SAR Interferometry Processing and Interpretation*, esa tm-19 feb 2007 ed. ESA, 2007.

[19] R. F. Hanssen, *Radar Interferometry: Data Interpretation and Error Analysis*. Dordrecht: Kluwer Academic Publishers, 2001.

[20] ——, *Radar Interferometry: Data Interpretation and Error Analysis*, 2nd ed. Heidelberg: Springer Verlag, 2005, in preparation.

[21] J. Muñoz Sabater, R. Hanssen, B. M. Kampes, A. Fusco, and N. Adam, "Physical analysis of atmospheric delay signal observed in stacked radar interferometric data," in *International Geoscience and Remote Sensing Symposium, Toulouse, France, 21–25 July 2003*, 2003, pp. cdrom, 4 pages.

[22] H. A. Zebker and J. Villasenor, "Decorrelation in interferometric radar echoes," *IEEE Transactions on Geoscience and Remote Sensing*, vol. 30, no. 5, pp. 950–959, Sep. 1992.

[23] V. Pascazio and G. Schirinzi, "Multifrequency insar height reconstruction through maximum likelihood estimation of local planes parameters," *Image Processing, IEEE Transactions on*, vol. 11, no. 12, pp. 1478–1489, Dec 2002.

[24] F. Gini, F. Lombardini, and M. Montanari, "Layover solution in multibaseline sar interferometry," *Aerospace and Electronic Systems, IEEE Transactions on*, vol. 38, no. 4, pp. 1344–1356, Oct 2002.

[25] S. Monti Guarnieri, A; Tebaldini, "Hybrid cramÉrŰrao bounds for crustal displacement field estimators in sar interferometry," *Signal Processing Letters, IEEE*, vol. 14, no. 12, pp. 1012–1015, Dec. 2007.

[26] Y. Rockah and P. Schultheiss, "Array shape calibration using sources in unknown locations–part ii: Near-field sources and estimator implementation," *Acoustics, Speech and Signal Processing, IEEE Transactions on*, vol. 35, no. 6, pp. 724–735, Jun 1987.

[27] I. Reuven and H. Messer, "A barankin-type lower bound on the estimation error of a hybrid parameter vector," *IEEE Transactions on Information Theory*, vol. 43, no. 3, pp. 1084–1093, May 1997.

[28] H. L. Van Trees, *Optimum array processing*, W. Interscience, Ed. New York: John Wiley & Sons, 2002.

[29] F. Rocca, "Synthetic aperture radar: A new application for wave equation techniques," *Stanford Exploration Project Report*, vol. SEP-56, pp. 167–189, 1987.

[30] A. Papoulis, *Probability, Random variables, and stochastic processes*, ser. McGraw-Hill series in Electrical Engineering. New York: McGraw-Hill, 1991.

[31] D. C. Ghiglia and M. D. Pritt, *Two-dimensional phase unwrapping: theory, algorithms, and software*. New York: John Wiley & Sons, Inc, 1998.

Geoscience and Remote Sensing New Achievements

Edited by Pasquale Imperatore and Daniele Riccio

ISBN 978-953-7619-97-8

Hard cover, 508 pages

Publisher InTech

Published online 01, February, 2010

Published in print edition February, 2010

Our planet is nowadays continuously monitored by powerful remote sensors operating in wide portions of the electromagnetic spectrum. Our capability of acquiring detailed information on the environment has been revolutionized by revealing its inner structure, morphology and dynamical changes. The way we now observe and study the evolution of the Earth's status has even radically influenced our perception and conception of the world we live in. The aim of this book is to bring together contributions from experts to present new research results and prospects of the future developments in the area of geosciences and remote sensing; emerging research directions are discussed. The volume consists of twenty-six chapters, encompassing both theoretical aspects and application-oriented studies. An unfolding perspective on various current trends in this extremely rich area is offered. The book chapters can be categorized along different perspectives, among others, use of active or passive sensors, employed technologies and configurations, considered scenario on the Earth, scientific research area involved in the studies.

How to reference

In order to correctly reference this scholarly work, feel free to copy and paste the following:

Stefano Tebaldini and Andrea Monti Guarnieri (2010). Methods and Performances for Multi-Pass SAR Interferometry, Geoscience and Remote Sensing New Achievements, Pasquale Imperatore and Daniele Riccio (Ed.), ISBN: 978-953-7619-97-8, InTech, Available from: http://www.intechopen.com/books/geoscience-and-remote-sensing-new-achievements/methods-and-performances-for-multi-pass-sar-interferometry

INTECH
open science | open minds